PNAS INAUGURAL ARTICLE | BIOCHEMISTRY OPEN ACCESS

Unwinding and spiral sliding of S4 and domain rotation of VSD during the electromechanical coupling in $Na_v1.7$

Gaoxingyu Huang[a,b,1], Qiurong Wu[c,1], Zhangqiang Li[c,1], Xueqin Jin[c,1], Xiaoshuang Huang[c], Tong Wu[c], Xiaojing Pan[c,2], and Nieng Yan[c,2,3]

This contribution is part of the special series of Inaugural Articles by members of the National Academy of Sciences elected in 2019.

Contributed by Nieng Yan; received May 27, 2022; accepted June 14, 2022; reviewed by Liang Feng and Vladimir Yarov-Yarovoy.

Voltage-gated sodium (Na_v) channel $Na_v1.7$ has been targeted for the development of nonaddictive pain killers. Structures of $Na_v1.7$ in distinct functional states will offer an advanced mechanistic understanding and aid drug discovery. Here we report the cryoelectron microscopy analysis of a human $Na_v1.7$ variant that, with 11 rationally introduced point mutations, has a markedly right-shifted activation voltage curve with $V_{1/2}$ reaching 69 mV. The voltage-sensing domain in the first repeat (VSD_I) in a 2.7-Å resolution structure displays a completely down (deactivated) conformation. Compared to the structure of WT $Na_v1.7$, three gating charge (GC) residues in VSD_I are transferred to the cytosolic side through a combination of helix unwinding and spiral sliding of $S4_I$ and ~20° domain rotation. A conserved WNΦΦD motif on the cytoplasmic end of $S3_I$ stabilizes the down conformation of VSD_I. One GC residue is transferred in VSD_{II} mainly through helix sliding. Accompanying GC transfer in VSD_I and VSD_{II}, rearrangement and contraction of the intracellular gate is achieved through concerted movements of adjacent segments, including S4-5_I, S4-5_{II}, $S5_{II}$, and all S6 segments. Our studies provide important insight into the electromechanical coupling mechanism of the single-chain voltage-gated ion channels and afford molecular interpretations for a number of pain-associated mutations whose pathogenic mechanism cannot be revealed from previously reported Na_v structures.

$Na_v1.7$ | cryo-EM structure | electromechanical coupling | resting VSD | pain

Significance

$Na_v1.7$ has been targeted for pain management for its well-established role in pain sensation. Hundreds of mutations of $Na_v1.7$ have been found in patients with pain disorders. Structures of $Na_v1.7$ captured in different conformations will reveal its working mechanism and facilitate drug discovery. Here we present the rational design of a $Na_v1.7$ variant, $Na_v1.7$-M11, that may be trapped in the closed-state inactivation conformation at 0 mV. Cryoelectron microscopy analysis of $Na_v1.7$-M11 reveals voltage-sensing domain in the first repeat (VSD_I) in the completely down conformation, VSD_{II} at an intermediate state, and the pore domain tightly closed. Structural comparison of $Na_v1.7$-M11 with the WT channel provides unprecedented insight into the electromechanical coupling details and affords mechanistic interpretation for a number of pain-related mutations.

The voltage-gated sodium (Na_v) channel $Na_v1.7$, encoded by *SCN9A*, is highly expressed in the pain-sensing neurons at the dorsal root ganglia and amplifies small membrane depolarizations for action potential firing. Loss of $Na_v1.7$ function can abolish pain sensation, while potentiation of its channel activity is associated with extreme pain disorders. $Na_v1.7$ has thus been targeted for developing next-generation pain killers (1–7). It is critical to capture the structures of $Na_v1.7$ in multiple functional states to facilitate drug discovery.

Unlike the homotetrameric K_v and bacterial Na_v channels, eukaryotic Na_v channels, as well as Ca_v channels, are made of one single-polypeptide chain that comprises four homologous transmembrane repeats (8, 9) (*SI Appendix*, Fig. S1). Similar to all other voltage-gated ion channels, Na_v channels contain two basic functional modules, the central ion-conducting pore domain (PD) and four flanking voltage-sensing domains (VSDs). Each VSD consists of four transmembrane segments (S1 to S4), among which S4 is responsible for detecting membrane potentials (9, 10). Four to six Arg or Lys residues, known as the gating charges (GC), occur at three-residue intervals on S4 (11). These positively charged residues face the cytosolic side at resting membrane potential, defined as the "down" or deactivated state. Upon membrane depolarization, GC residues move toward the extracellular side to reach an "up" or activated state (12).

Two to three GCs are transferred in each VSD during Na_v channel activation (13). The conformational shifts of the VSDs are allosterically transmitted to the PD to control pore gating, a process known as the electromechanical coupling (EMC) (14). The primary steps in an EMC cycle of Na_v channels include transition from the resting to the activated state in response to membrane depolarization (activation), closure of the channel in millisecond-scale after activation (fast inactivation), and return to the resting state upon hyperpolarization (deinactivation) (15).

Prior to structural elucidation, decades of electrophysiological, biophysical, and pharmacological characterizations have predicted the following conformational features for the major states (15, 16). At the resting state, the VSDs are "down" and the PD is closed. The activated state has opposite conformations, with "up" VSDs and conductive PD. Na_v channels can inactivate through both fast and slow mechanisms. An inactivated channel is nonconductive and the VSDs are at least partially up because of the

Author contributions: Z.L., X.P., and N.Y. designed research; G.H., Q.W., Z.L., X.J., X.H., T.W., and X.P. performed research; G.H., Q.W., Z.L., X.J., X.H., T.W., X.P., and N.Y. analyzed data; and X.P. and N.Y. wrote the paper.

Reviewers: L.F., Stanford University; and V.Y.-Y., University of California, Davis.

The authors declare no competing interest.

See Profile, e2210772119, in vol. 119, issue 33.

[1]G.H., Q.W., Z.L. and X.J. contributed equally to this work.

[2]To whom correspondence may be addressed. Email: panxj@tsinghua.edu.cn or nyan@princeton.edu.

[3]Present address: Department of Molecular Biology, Princeton University, Princeton, NJ 08544.

This article contains supporting information online at http://www.pnas.org/lookup/suppl/doi:10.1073/pnas.2209164119/-/DCSupplemental.

Published July 25, 2022.

depolarized membrane potential. Whereas fast inactivation is executed by the Ile/Phe/Met (IFM) motif, which is positioned on the short linker between repeats III and IV (the III-IV linker) (17), the determinants and mechanism for slow inactivation remains elusive.

As the resting state of WT Na_v channels is held by a strong electric field across the membrane and the activated state is only transient, the inactivated conformation may represent the most stable state in the absence of transmembrane voltages or gating modifiers. Indeed, the majority of the resolved structures of unmodified eukaryotic Na_v channels shares a similar conformation that is featured with loosely closed PD and up VSDs, consistent with the inactivated state. Of note, the IFM motif wedges into a receptor site that was first discovered in the structure of $EeNa_v1.4$ ($Na_v1.4$ homolog from electric eel) and then observed in all human and rat Na_v channel structures (18–26). Based on the structures and reported functional characterizations, we proposed a "door wedge" allosteric blocking mechanism for fast inactivation, wherein insertion of the IFM motif in the accommodation site that is at the corner outside $S6_{III}$ and $S6_{IV}$ drives the contraction of the S6 helical bundle to close the intracellular gate (18).

The outlier in the Na_v structure gallery is Na_vPaS, the first eukaryotic Na_v channel whose structure was resolved (27). The GC residues in VSDs I, II, and IV of Na_vPaS are 1 to 1.5 helical turns lower than the corresponding ones in the vertebrate Na_v structures; the PD is tightly closed without fenestrations; and the S4-5 constriction ring is more contracted. The most distinctive feature occurs in the III-IV linker, which cofolds with a globular carboxy terminal domain, keeping the IFM-corresponding residues far from the binding site. Unfortunately, the functional state of the Na_vPaS structure cannot be defined due to the difficulty of recording Na_vPaS.

To dissect the EMC of Na_v channels, various strategies have been employed to lock the channels in different states. A chimera was generated by grafting VSD_{IV} and eight residues on the adjacent $S5_I$ from $Na_v1.7$ to the scaffold of Na_vPaS. The S4 segment in the grafted VSD_{IV} is one helical turn higher than that in the original Na_vPaS-VSD_{IV}. Upon binding to AaH2, an α-scorpion toxin, two GC residues are transferred toward the cytosolic side (28). Similarly, the $S4_{IV}$ segment of rat $Na_v1.5$ also moves down by two GC residues in the presence of another scorpion toxin LqhIII (29). Despite the conformational changes of VSD_{IV} in these channels, the PD remains nearly unchanged, preventing mechanistic dissection of the EMC.

Here we report structure-based engineering of a functional $Na_v1.7$ variant that exhibits substantially right-shifted voltage dependence for activation. Structural comparison of this variant, in which VSD_I is in a completely down state, with WT $Na_v1.7$ (26) reveals multimodal conformational changes of VSD_I and VSD_{II} that are propagated to intracellular gating through crosstalk between adjacent segments. A conserved WNΦΦD motif (Φ for hydrophobic residue) on the $S3_I$ segment is discovered to stabilize the down conformation of VSD_I.

Results

Structure-Guided Engineering of Right-Shifting $Na_v1.7$ Variants. Toward the goal of capturing $Na_v1.7$ in a resting state, we set out to introduce point mutations that might lead to the right shift of activation and steady-state inactivation threshold beyond 0 mV. Mutations were selected based on the following rationales.

First, the lack of fenestration on the PD of Na_vPaS (30) suggested that more energy, equivalent of more depolarized voltage, may be required to disrupt the interactions of the pore-forming segments for channel opening. Indeed, sequence comparison of Na_vPaS and human Na_v channels reveals that the former contains larger number of bulky residues on S5 and S6 in repeats II and III. We thereby replaced the small fenestration-constituting residues in $Na_v1.7$ with the corresponding larger ones from Na_vPaS (Fig. 1*A* and *B* and *SI Appendix*, Fig. S1). A combination of nine point mutations—L866F, T870M, and A874F on $S5_{II}$; V947F, M952F, and V953F on $S6_{II}$; and V1438I, V1439F, and G1454C on $S6_{III}$ (the resulting variant named as $Na_v1.7$-M9)—shifted the $V_{1/2}$ of the activation curve of $Na_v1.7$ from -26.00 ± 0.26 mV to -1.59 ± 0.33 mV and the inactivation curve from -69.21 ± 0.37 mV to -60.40 ± 0.56 mV (Fig. 1*B* and *C* and *SI Appendix*, Fig. S2*A* and Table S1).

Second, numerous disease-related mutations have been characterized to cause positive shift of the activation voltage. Inspired by our structural analysis of $Na_v1.5$ disease mutations (24, 25), two right-shifting point mutations, E156K on $S2_I$ and G779R on $S2_{II}$ (31, 32), were introduced to $Na_v1.7$-M9, and the resulting variant $Na_v1.7$-M11 exhibited a markedly right-shifted and less steep activation curve with the $V_{1/2}$ reaching 69.37 ± 0.80 mV. No current could be recorded below 30 mV for $Na_v1.7$-M11. The inactivation curve is also right-shifted with a reduced slope, $V_{1/2}$ reaching -49.44 ± 0.95 mV (Fig. 1*C* and *SI Appendix*, Fig. S2*A* and Table S1).

When the preholding potential is set at −120 mV, $Na_v1.7$ completely activates at 0 mV, followed by fast inactivation (Fig. 1*C* and *SI Appendix*, Fig. S2*A* and Table S1). But when held for prolonged time at more depolarized potentials, such as −70 mV or −50 mV, the WT channel can enter closed-state inactivation (CSI) (*SI Appendix*, Fig. S2*B*) (33, 34). Our electrophysiological characterizations suggest that while $Na_v1.7$-WT and $Na_v1.7$-M9 likely display conformations of open-state inactivation (OSI) after protein extraction and purification in the absence of any electric field, $Na_v1.7$-M11 may be trapped in the CSI state. To examine potential conformational differences between the two states, we set out to solve the structure of $Na_v1.7$-M11.

Two Distinct Conformations of VSD_I in $Na_v1.7$-M11. Following our established protocols (26), a three-dimensional (3D) electron microscopy (EM) reconstruction for $Na_v1.7$-M11 in the presence of the β1 and β2 subunits were obtained at an averaged resolution of 2.8 Å of 912,322 selected particles. Unlike $Na_v1.7$-WT, VSD_I was only resolved to 8 to 10 Å at this stage. Combining maximum-likelihood–based classification and local refinement, two classes of 3D reconstructions were obtained with overall resolutions of 2.7 Å (class I) and 2.8 Å (class II) (Fig. 1*D* and *SI Appendix*, Figs. S3 and S4 and Table S2). The two classes only diverge in VSD_I, which rotates by ∼20° around the PD (Fig. 1*D* and *SI Appendix*, Fig. S5). Structural comparison shows that class II is more similar to WT (*SI Appendix*, Fig. S5). We will mainly focus on class I, whose overall resolution reaches 2.7 Å (Fig. 1*E*), for analysis. For simplicity, $Na_v1.7$-M11 or M11 hereafter refers to the class I structure if not otherwise indicated.

When the structures of M11 and WT are superimposed, the extracellular loops, the extracellular half of the PD, VSD_{III} and VSD_{IV} remain identical, while all other segments, exemplified by VSD_I, undergo conformational changes to different degrees (Fig. 1*F* and Movie S1). In the following, we will illustrate the major structural rearrangements from WT to M11 and present an analysis of the coupling mechanism. Movements of structural segments toward the extracellular and intracellular side

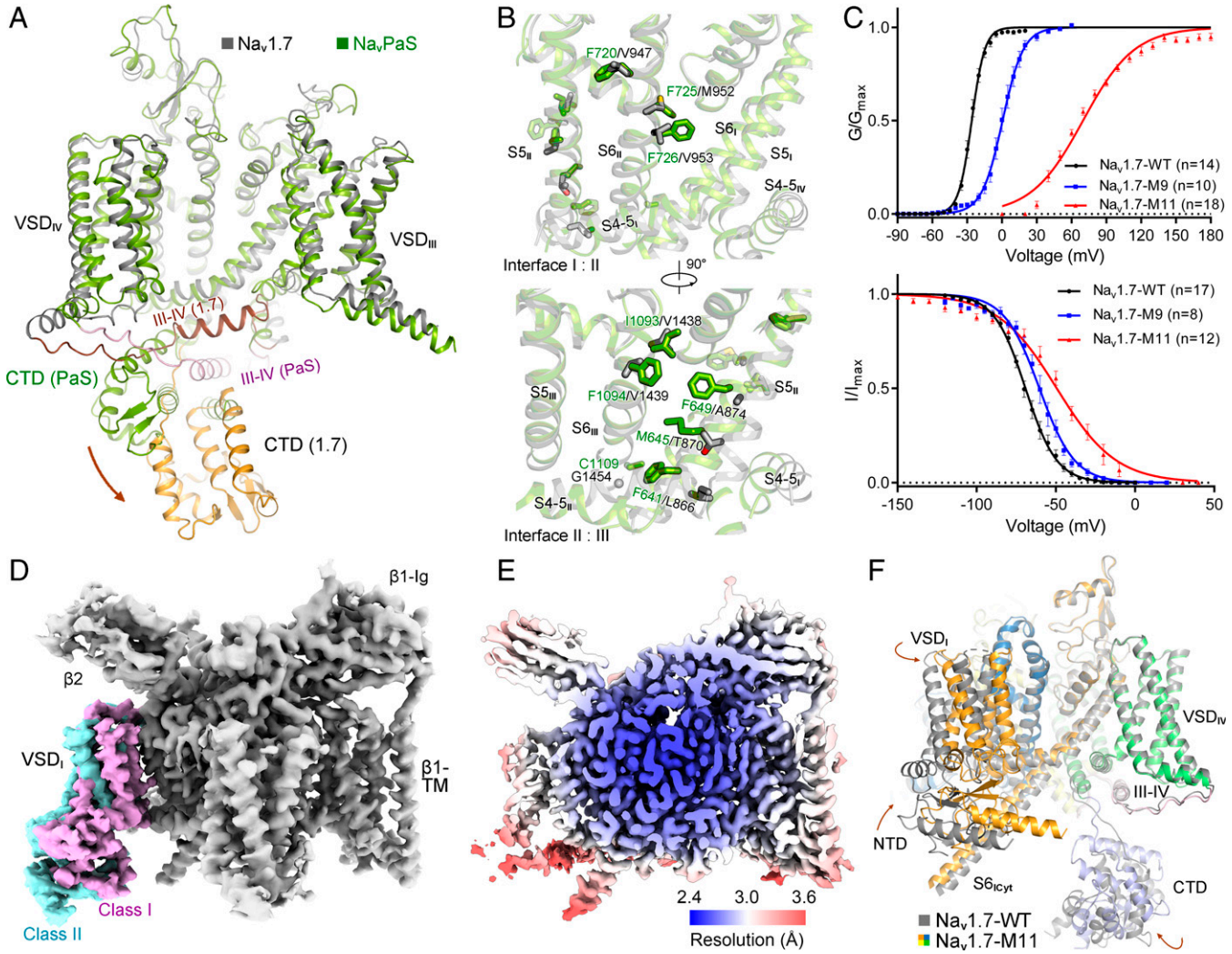

Fig. 1. A rationally designed Na$_v$1.7 variant with right-shifted voltage-dependence for activation and inactivation displays marked conformational shifts from the WT channel. (*A*) Distinct conformations of WT human Na$_v$1.7 and Na$_v$PaS. Shown here is a side view of the superimposed α subunit of Na$_v$1.7 and Na$_v$PaS (PDB ID codes: 7W9K and 6A95, respectively). The brown arrow indicates the swing of the carboxy terminal domain (CTD) from Na$_v$PaS to Na$_v$1.7. (*B*) Structure-guided introduction of mutations that may strengthen the interactions between adjacent repeats in the PD of Na$_v$1.7. Nine small residues on S5$_{II}$, S6$_{II}$, and S6$_{III}$ in Na$_v$1.7 are replaced by the corresponding ones in Na$_v$PaS, which contains more bulky residues on the interface of adjacent repeats. The Na$_v$1.7 variant containing L866F, T870M, A874F, V947F, M952F, V953F, V1438I, V1439F, and G1454C is designated Na$_v$1.7-M9. (*C*) Right shift of both activation and inactivation curves of Na$_v$1.7 variants. $V_{1/2}$ of the activation curve for Na$_v$1.7-M9 is shifted from −26.02 ± 0.24 mV to 0.55 ± 0.43 mV, and that of the inactivation curve changes from −69.21 ± 0.37 mV to −60.40 ± 0.56 mV. Two additional mutations, E156K on S2$_I$ and G779R on S2$_{II}$, led to a pronounced right shift of the activation threshold with the $V_{1/2}$ reaching 69.37 ± 0.80 mV. This variant, designated Na$_v$1.7-M11, was applied for cryo-EM structural analysis. Data points are presented as mean ± SEM and *n* is the number of recorded cells. Statistical significance was assessed using one-way ANOVA analysis. (*D*) Two distinct conformations of VSD$_I$ were observed in the 3D EM reconstructions of Na$_v$1.7-M11. For simplicity, the label Na$_v$1.7-M11 or M11 refers to class I hereafter, unless otherwise indicated. (*E*) Heat map for resolution distribution of M11. Local resolutions were calculated in RELION 3.0. (*F*) Overall structural shifts between M11 and WT. Shown here is a side view of the superimposed structures. Structures of the β1 and β2 subunits are omitted in all structure figures. The brown arrows indicate the conformational shifts from WT (gray) to M11 (domain colored). Movies S1–S4 illustrate the conformational changes presented in different figures. Maps were prepared in Chimera (48) and structure figures were prepared in PyMol (49).

will be described as upward and downward, respectively, and motions toward the center and periphery of the channel in the membrane-parallel plane will be described as inward and outward, respectively.

Completely Deactivated (Down) VSD$_I$. VSD$_I$ contains four GC residues: Arg214 (R2), Arg217 (R3), Arg220 (R4), and Lys223 (K5). In the context of the overall structural comparison of the α-subunit from WT and M11, VSD$_I$ pivots around the extracellular contact point between S1$_I$ and the PD (Fig. 2*A* and *B*). In addition to a ∼20° domain-wise rotation of VSD$_I$, the movement of S4$_I$ combines several modes of structural transitions, resulting in the transfer of three GC residues, R2 to R4, across the occluding residue, Tyr163 on S2$_I$, to the intracellular side in M11 (Fig. 2*C* and *D* and Movies S1–S3). It is noted that rotation of VSD$_I$ is also observed in the cryo-EM structures of Na$_v$1.8, in which multiple conformations for VSD$_I$ were resolved. Despite substantial structural rearrangements, all the VSD$_I$ conformers in Na$_v$1.8 remain in the up states (35).

S4$_I$ undergoes a spiral and tilted sliding toward the cytosol from WT to M11 with the backbone traversing the membrane by 11 to 14 Å (Fig. 2*C* and *D*). Unexpectedly, the last one-and-half helical turns of S4$_I$ in WT, consisting of residues $_{222}$LKTISV$_{227}$, unwind to become an extended linker that connects S4$_I$ and S4-5$_I$. The extracellular end of S4$_I$ is also unwound by half a helical turn. Together, S4$_I$ in WT comprises two more helical turns than that in M11 (Fig. 2*C* and *D*).

When individual VSD$_I$ is compared between WT and M11, there is no internal movement among S1–S3$_I$ segments. They rotate as a rigid body accompanying the gating charge transfer (Fig.

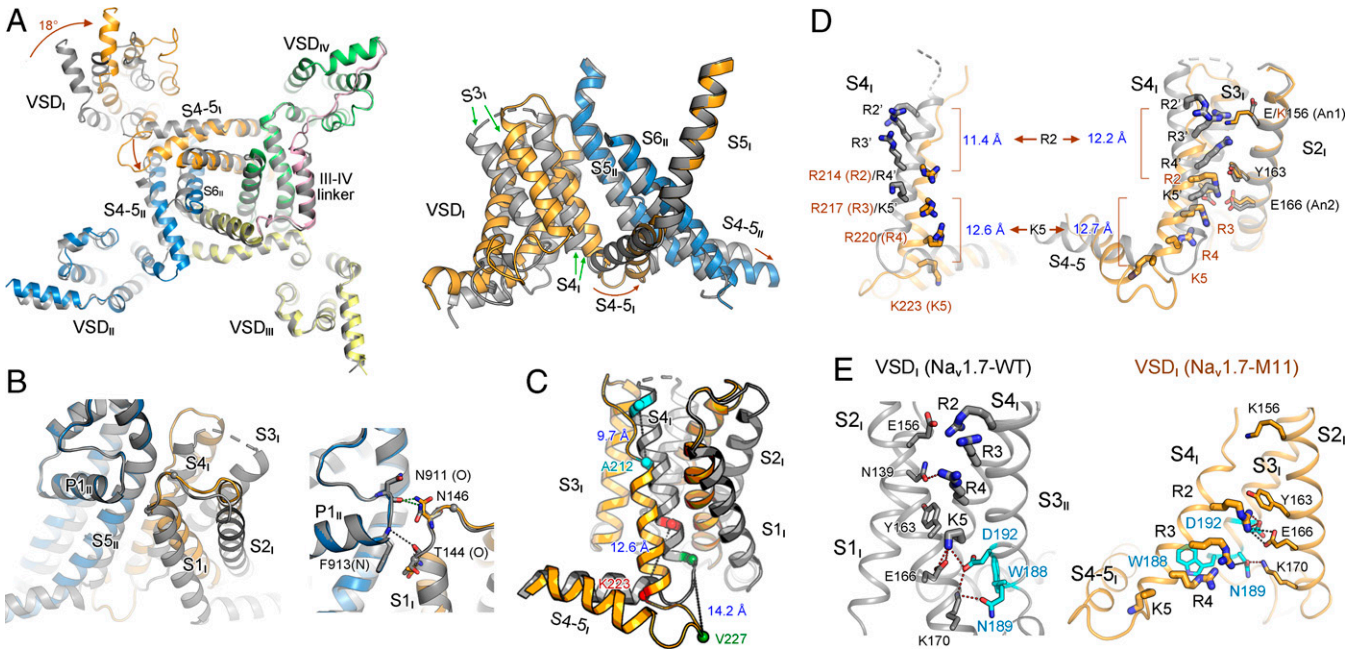

Fig. 2. Multimodal conformational changes of VSD$_I$ between its up and down states. (*A*) Large-degree conformational changes between M11 and WT mainly occur in repeats I and II. (*Left*) An intracellular view of the superimposed α subunits from M11 (domain colored) and WT (dark gray). Intracellular segments are omitted for visual clarity. (*Right*) A side view of the rotation of VSD$_I$ and the ensuing S4-5$_I$ segment. Brown arrows indicate the shift of the corresponding segments from WT to M11. (*B*) The pivot for VSD$_I$ rotation. VSD$_I$ swings around the contact between the extracellular tips of S1$_I$ and P1$_{II}$. (*Right*) The interactions between the carbonyl oxygen of Thr144 and the side chain of Asn146 in VSD$_I$ with main-chain groups of the starting turn of P1$_{II}$ helix are preserved in M11 and WT, representing the pivoting point for VSD$_I$ rotation. (*C*) Dissection of conformational changes of VSD$_I$ between the up (WT) and down (M11) states. An enlarged view of the superimposed VSD$_I$ and the S4-5$_I$ linker from *A* is shown. Structural shifts of S4$_I$ combine helical unwinding, tilted sliding, and axial rotation. Cα atoms of the residues that mark the termini of S4$_I$ helices in the two structures are shown as spheres. The linear displacement of the Cα atoms of these residues in the context of overall structural comparison are indicated. S1–S3$_I$ segments rotate around S4$_I$. (*D*) Downward transfer of three GC residues in VSD$_I$ from WT to M11. The linear displacement of the Cα atoms of R2 and K5 residues, which mark the two ends, in the context of overall structural comparison (*Left*) and individual VSD$_I$ comparison (*Right*) are indicated. The WT residues are labeled with apostrophe. (*Right*) When the structures of VSD$_I$ are individually compared, S1–S3 can be completely overlaid. (*E*) A conserved WNΦΦD motif on the cytoplasmic terminus of S3$_I$ stabilizes the GC residues in the down conformation of VSD$_I$. Φ stands for hydrophobic residues. (*Left*) Coordination of GC residues in the up VSD$_I$ in WT. S1$_I$ is omitted for visual clarity. (*Right*) R2–R4 are stabilized by the WNΦΦD motif in the down VSD$_I$ in M11. The top GC residue R2 forms cation–π interaction with the occluding Tyr163 on S2$_I$ and electrostatic interaction with Asp192 in the WNΦΦD motif. Red and black dashes indicate distances of 2.8 to 3.5 Å and 4.5 to 5.5 Å, respectively.

2*D*). The driving force for the rotation of S1–S3$_I$ appears to be the sliding motion and the secondary structural shift of S4$_I$ on the extracellular side. When the extracellular segment of S4$_I$ is unwound from WT to M11, S3$_I$ is dragged toward the PD. When S4$_I$ moves upward, the restored helical turns, which requires more space, pushes S3$_I$ away (Fig. 2*C* and *D* and Movie S2).

Due to the unwinding of the cytosolic helical turns of S4$_I$, the ensuing S4-5$_I$ linker, which rotates toward S4-5$_{II}$, remains at similar height in these two structures despite the pronounced downward translocation of S4$_I$. Therefore, the different directions of motions, vertical for S4$_I$ and horizontal for S4-5$_I$, are reconciled through secondary structural transformation of S4$_I$ (Fig. 2*A* and *C* and Movie S2).

The structure of VSD$_I$ in Na$_v$1.7-M11 represents a VSD in the completely deactivated or resting state, as all its GC residues face the cytosolic side. Compared to the up state in the WT, GC residues are coordinated by a different set of polar residues (Fig. 2*E*). In the down conformation, the top R2 is most stably anchored, through cation–π interaction with the occluding Tyr163 on S2$_I$ and polar interaction with the invariant Asp192 on S3$_I$. R3 is out of reach for direct hydrogen bonds (H-bonds) with any surrounding residues, but it may be coordinated by Glu166 on S2$_I$ and Asn189/Asp192 on S3$_I$ through water-mediated H-bonds. R4 may also form water-mediated H-bonds with Asp186 on the S2-3$_I$ linker and Asn189 on S3$_I$, in addition to cation–π interaction with Trp188 (Fig. 2*E*, *Right*).

Among the GC-coordinating residues in the down state, Tyr163, Glu166, and Asp192 constitute the conserved charge transfer center (36). Of particular note, Asp192 and its preceding sequence on the cytosolic end of S3$_I$, $_{186}$DPWNWL$_{191}$D$_{192}$, are invariant in all VSD$_I$ of human Na$_v$ channels (*SI Appendix*, Fig. S1). Sequence analysis shows that the WNΦΦD (Φ representing hydrophobic residues) motif is conserved in all VSDs except VSD$_{III}$, where Asn is replaced by Cys (*SI Appendix*, Fig. S1). Supporting the functional significance of this motif, Na$_v$1.1 variants that each contain a single point substitution—W190R, N191K, N191Y, D194G, and D194N—are all associated with epileptic encephalopathy, early infantile, 6 (EIEE6), one of the most severe generalized epilepsies (37–40). Structure of Na$_v$1.7-VSD$_I$ in the down conformation thus reveals the molecular basis for the functional significance of this conserved motif.

One GC Transfer in VSD$_{II}$. The structures of VSD$_{II}$ are nearly identical in the two classes of Na$_v$1.7-M11, except for minor rotation of side chains (*SI Appendix*, Fig. S5*E*). One GC residue moves down from that in WT, placing both K5 and K6 below the occluding Phe787 (Fig. 3*A*). The GC transfer is also accompanied with a subtle but discernible overall domain rotation (Fig. 3*A* and Movie S2). The transfer of one GC is achieved through helix sliding of S4$_{II}$ by about 5-Å displacement of the backbone (Fig. 3*B* and Movie S2). There is no secondary structural transition of S4$_{II}$. In contrast to the relatively minor shift of S4$_{II}$, the S4-5$_{II}$ segment undergoes a marked dislocation. The entire helix drops down almost parallelly to the cytoplasm by ∼6 Å (Fig. 3*A*).

Coordination of the GC residues in VSD$_{II}$ in this conformation mainly involves water-mediated electrostatic interactions between

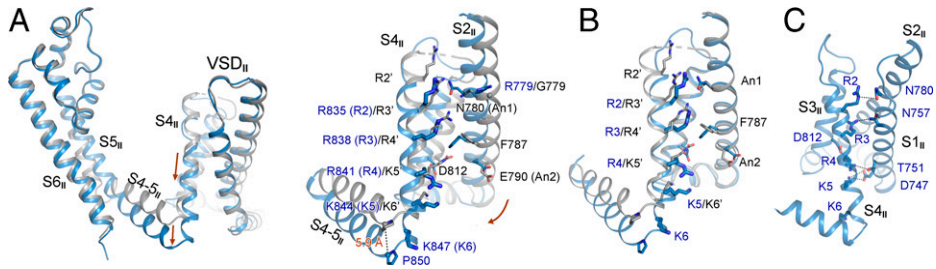

Fig. 3. Structural changes of VSD$_{II}$ between Na$_v$1.7-M11 and Na$_v$1.7-WT. (*A*) Conformational changes of S1–S6 in repeat II between M11 and WT. (*Left*) The two structures are superimposed as in Fig. 2*A*. Shown here is a side view of the superimposed repeat II. Although the shift of VSD$_{II}$ is to a smaller degree than that of VSD$_I$, the S4-5$_{II}$, S5$_{II}$, and S6$_{II}$ segments display pronounced changes. (*Right*) VSD$_{II}$ undergoes a minor rotation around the PD accompanying the transfer of one GC residue. In the WT channel (dark gray), R2′–R4′ of VSD$_{II}$ are above the occluding residue Phe787. In M11 (blue), only R2 and R3 remain above. (*B*) GC transfer in VSD$_{II}$ is mainly achieved through helix sliding of S4$_{II}$. S1$_{II}$ is omitted for visual clarity. (*C*) Coordination of the GC residues in M11-VSD$_{II}$ by polar residues. Potential direct and water-mediated hydrogen bonds are indicated by black dashed lines.

R2-K5 and several polar residues on S1$_{II}$ (Fig. 3*C*). The top R2 interacts with Asn780 on S2$_{II}$. R3 is out of reach of any surrounding residues for H-bond formation, but it may be coordinated by Asn757 on S1$_{II}$ through water-mediated H-bonds. R4 may form direct or water-mediated H-bonds with Thr751 on S1$_{II}$ and Asp812 on S3$_{II}$, respectively. K5 is stabilized by Asp747 on S1$_{II}$.

A Tightly Closed PD in Na$_v$1.7-M11. In addition to the conformational shifts of VSD$_I$ and VSD$_{II}$, M11 lacks the detergent molecule that penetrates the intracellular gate, a shared feature in all structures of ligand-free WT human Na$_v$ channels. Indeed, calculation of the channel permeation path shows that the radius of the constriction point of the intracellular gate is only ~0.9 Å

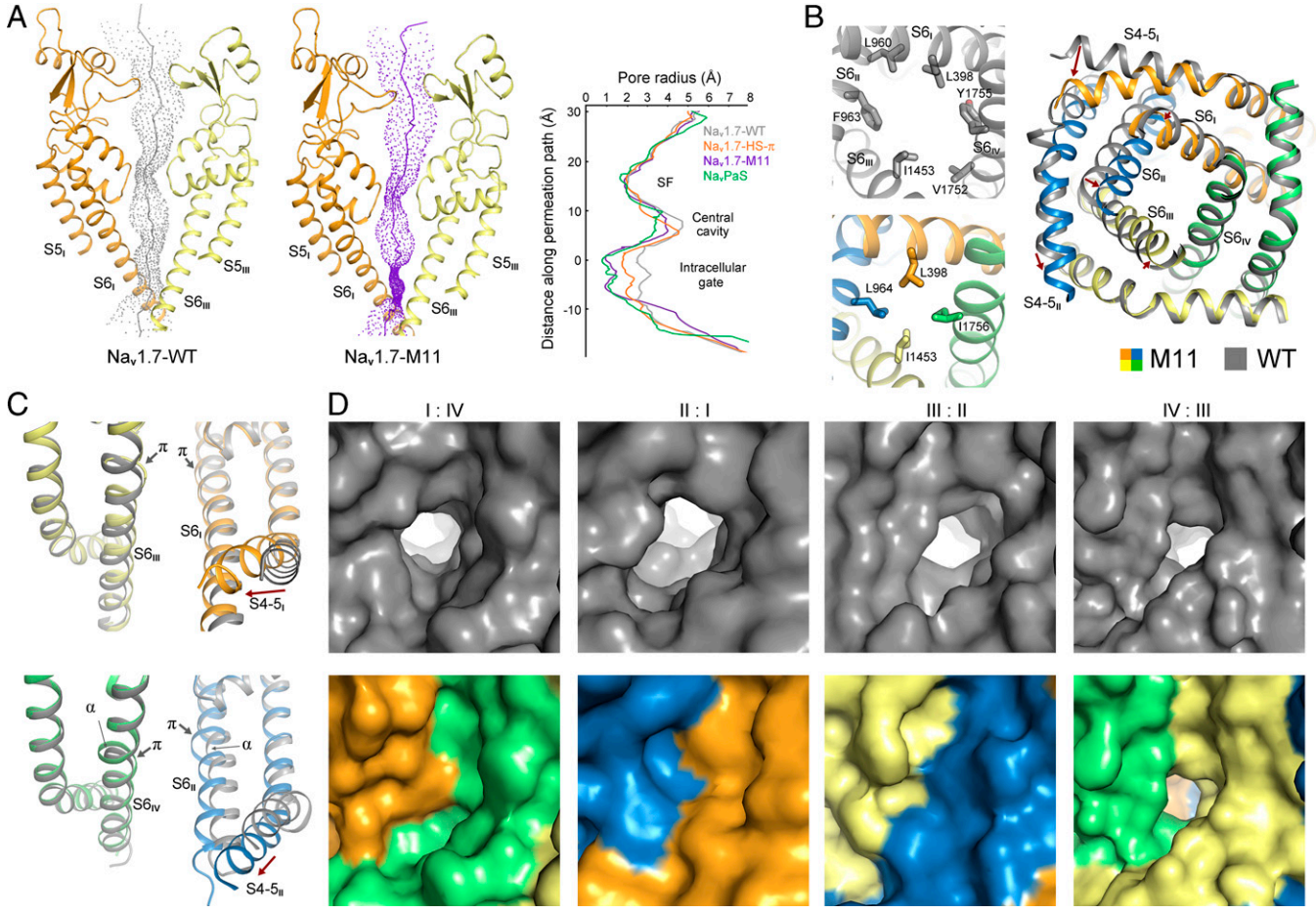

Fig. 4. The PD of Na$_v$1.7-M11 is substantially contracted compared to the WT channel. (*A*) The radius of the intracellular gate of M11 is reduced by over 1.5 Å compared to WT. The permeation paths of WT and M11 were calculated in HOLE (50). The corresponding pore radii are compared (*Right*). HS–π refers to the structure of HWTX-IV and saxitoxin-bound Na$_v$1.7 (PDB ID code 7W9P). Na$_v$PaS refers to the structure in the presence of Dc1a and tetrodotoxin (PDB code ID 6A95). HS–π and Na$_v$PaS are included to indicate the level of PD contraction from WT to M11. (*B*) Contraction of the pore-forming segments of M11. (*Left*) Comparison of the intracellular gate of WT (*Upper*) and M11 (*Lower*). The gating residues are shown as sticks. (*Right*) An intracellular view of the superimposed PD of M11 and WT. Shifts of the corresponding segments from WT to M11 are indicated by red arrows. Contraction of the gate is mainly caused by rotation and inward motion of S6$_{II}$. (*C*) All the S6 segments in M11 contain π helical turns. Side views of the PD from diagonal repeats of superimposed WT and M11 are presented. In WT channel, only S6$_I$ and S6$_{III}$ possess π-helical turns. (*D*) Only one small fenestration remains on the interface of repeats III and IV in the structure of M11. Corresponding side views of the surface presentation of the four side walls of the PD in WT (*Upper*) and M11 (*Lower*) are shown.

in M11, shortened by ∼1.5 Å from that of the WT channel. It is also narrower than that of $Na_v1.7$(E406K) in the presence of Huwentoxin-IV (designated $Na_v1.7$-HS) (26). The overall contour of the permeation path of M11 is largely similar to that of Na_vPaS, although their PD segments still deviate considerably (Fig. 4*A* and *SI Appendix*, Fig. S6).

The composition of gating residues from the S6 tetrahelical bundle is different between WT and M11. In WT, the contour of the intracellular gate is of an oval shape, constituted by six residues: Leu398, Leu960, Phe963, Ile1453, Val1752, and Tyr1755. In contrast, four residues—Leu398, Leu964, Ile1453, and Ile1756—interact closely to seal the intracellular gate of M11 (Fig. 4*B*, *Left*, and Movie S3). Closure of the intracellular gate is a result of swing motion of $S6_{II}$ and $S6_{III}$ as well as α→π transition of $S6_{II}$ and $S6_{IV}$ (Fig. 4*B*, *Right*, Fig. 4*C*, and Movie S3). In M11, all four S6 segments contain one π helical turn in the middle (Fig. 4*C*). Accompanying these rearrangements, the central cavity shrinks (Fig. 4*A*) and the side walls of the PD other than the III and IV interface have no fenestrations (Fig. 4*D*).

In the following session, we will analyze the allosteric coupling of pore gating with the structural shifts of VSD_I and VSD_{II} through cross-talk of adjacent segments in all repeats.

EMC through Concerted Motions of Adjacent Segments. As VSD_I undergoes the most dramatic conformational transition, we attempt to delineate the route of EMC from VSD_I to the intracellular gate. Three coupling nodes are found, one between S4-5_I and the joint connecting S4-5_{II} and $S5_{II}$ (Fig. 5*A*–*C*), next between $S5_{II}$ and $S6_{II}$ (Fig. 5*D*), and finally the cross-talk among all S6 segments (Fig. 5*E*–*G*). Movement of $S4_{II}$ may also contribute to the shift of S4-5_{II} and $S5_{II}$.

In all previously reported structures of eukaryotic Na_v channels, Na_vPaS included, S4-5_{II} (forearm) and $S5_{II}$ (upper arm) are connected by a sharp turn (elbow). In M11, the "arm" extends forward and the elbow becomes a smoothly curved helix (Fig. 5*A*). This structural transition appears to be mainly driven by the shift of S4-5_I, whose N terminus moves toward the elbow by a displacement of over 6 Å (Fig. 5*B*). The distance between the N terminus of S4-5_I and the cytoplasmic end of $S5_{II}$ remains nearly unchanged despite the marked conformational difference between WT and M11, demonstrating coupled motions.

The coupling is mediated by a conserved hydrophobic cluster composed of Ile234, Val235, and Leu238 on S4-5_I and Leu869 and Val872 on $S5_{II}$ (Fig. 5*C*, *SI Appendix*, Fig. S1, and Movie S2). While S4-5_I mainly pushes the elbow and $S5_{II}$, the downward sliding of $S4_{II}$ may drag the overall S4-5_{II} helix to sink toward the cytoplasmic side (Fig. 3*A*). As there is only one GC transfer in VSD_{II}, the physiological coupling between $S4_{II}$ and S4-5_{II} awaits further examination.

Tilting of $S5_{II}$ directly drives $S6_{II}$ movement (Fig. 5*D* and Movie S3). If $S6_{II}$ had not shifted concertedly, there would be steric clashes between residues on $S6_{II}$ and $S5_{II}$ (Fig. 5*D*). Motions of these repeat II segments further propagate to $S6_{III}$; the latter has to tilt toward $S6_{IV}$ to avoid clash with residues on S4-5_{II}, $S5_{II}$, and $S6_{II}$ (Fig. 5*E*). The middle turn of $S6_{IV}$ undergoes an α→π transition, replacing Ile1757 with a smaller Ala1757 to avoid collision with the shifted Ile1457 on $S6_{III}$ (Fig. 5*F*). Finally, to avoid colliding with Tyr1755 on $S6_{IV}$, $S6_I$ slightly moves inward and the aromatic rings of Phe387 and Phe391 rotate up, eliminating the fenestration between repeats I and IV (Fig. 5*G*). It is noted that the coupled

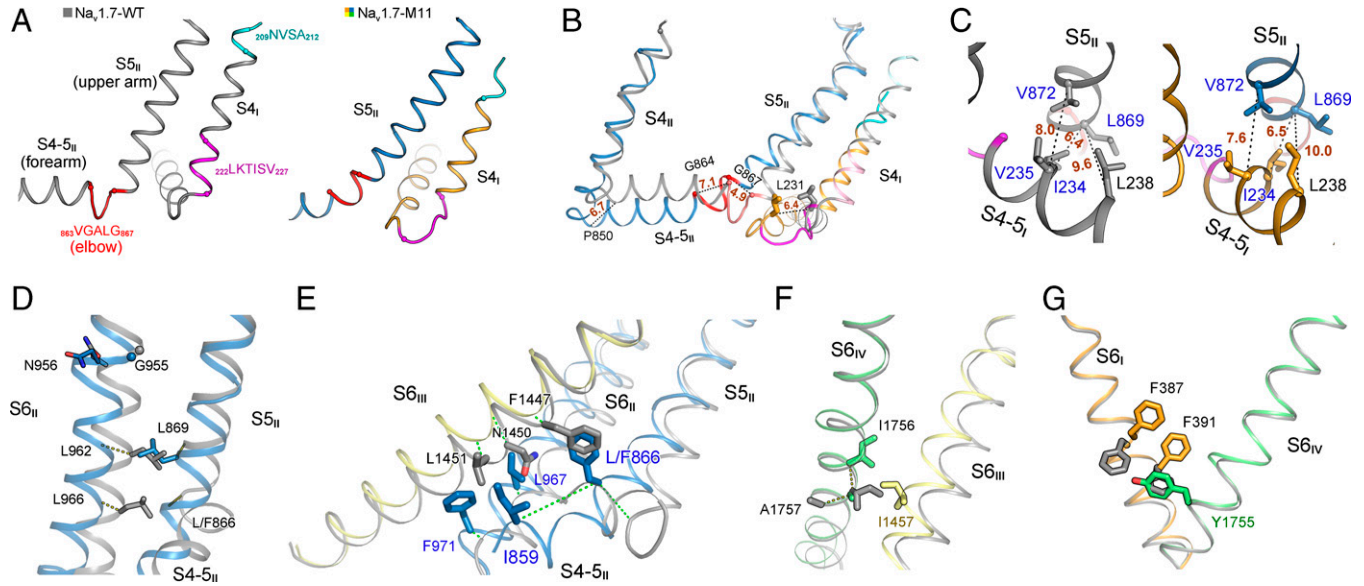

Fig. 5. Electromechanical coupling of GC transfer to intracellular gating through concerted motions of adjacent segments. (*A*) Prominent secondary structure transition of the adjacent $S4_I$ and S4-5_{II} segments. The corresponding sequences that undergo helical winding/unwinding between WT and M11 are highlighted with the same color in the two structures. Of note, the unwound sharp turn (elbow, colored red) between S4-5_{II} and $S5_{II}$ in WT is transformed to a curved helical turn in M11. (*B*) Concerted structural shifts of S4-5_I segments with the adjacent S4-5_{II} and $S5_{II}$ segments. Structures of WT (gray) and M11 (domain colored) are superimposed as in Fig. 2*A*. Displacement of the Cα atoms of terminal residues on $S4_I$, S4-5_I, S4-5_{II}, and $S5_{II}$ are indicated with dashed lines and labeled in ångstroms. (*C*) A hydrophobic cluster on the interface of S4-5_I and $S5_{II}$ couples the concerted motions of these two segments. The distances between the indicated Cα atoms are labeled in ångstroms. (*D*) Concerted motions of $S6_{II}$ and $S5_{II}$. The Cα atoms of the corresponding residues in the superimposed M11 and WT structures are connected by dashed lines to indicate their displacements. Leu962 and L966 on $S6_{II}$ would respectively clash with Leu869 and Leu866 (mutated to Phe in M11) on $S5_{II}$ had $S6_{II}$ not moved concertedly. (*E*) $S6_{III}$ is pushed inwardly by S4-5_{II} and $S6_{II}$. Displacements of the Cα atoms of the corresponding residues in M11 and WT are indicated by dashed lines. Representative residues in WT and M11 are shown to indict potential clashes should $S6_{III}$ not move accordingly. (*F*) Concerted motions of $S6_{III}$ and $S6_{IV}$. $S6_{IV}$ undergoes an α→π transition that avoids clash between Ile1457 and Ile1756. (*G*) The subtle shift of $S6_{IV}$ leads to local change of $S6_I$. Rotation of the aromatic rings of Phe387 and Phe391 seals the fenestration on the interface of repeats I and IV (Fig. 4*D*). It is noted that the conformational changes from WT to M11 depicted in *F* and *G* are nearly identical to those of $Na_v1.7$ upon HWTX-IV binding to VSD_{II} (26).

conformational changes from $S6_{III}$ to $S6_I$ described in Fig. 5*F* and *G* are identical with those observed in $Na_v1.7$ upon toxin binding to VSD_{II} (26).

Substantial Rearrangement of the Interface between VSD_I and the PD. The motions of VSD_I and VSD_{II} relative to the PD lead to the rearrangement of their respective interface with the neighboring pore segments (*SI Appendix*, Fig. S7). As $S5_{III}$ remains unchanged and $S4_{II}$ only undergoes sliding by one helical turn, their interface is mediated by a similar set of residues except for the shift of their relative positions (Movie S2). In contrast, the interface of VSD_I and the PD undergoes substantial rearrangements. The contact between VSD_I and $S5_{II}$ is more extensive in M11 than in WT, with a dozen additional interacting residues (Fig. 6*A* and *SI Appendix*, Fig. S7).

Discussion

Structural Insight into Mutations in Pain Disorders. Structural comparison of WT and M11 affords important mechanistic insight into a number of disease-causing mutations that could not be interpreted from previous structures (SI *Appendix*, Table S3 and Movie S4). Instead of enumerating all concerned residues, we select several representative ones that are associated with primary erythermalgia (PERYTHM).

The PERYTHM mutation F216S causes left shift of the activation $V_{1/2}$ by 11 mV (41). The functional role of Phe216, which is positioned on the second helical turn of $S4_I$ and points to the lipid bilayer in previous structures, was unclear. In the present deactivated VSD_I, Phe216, which undergoes a marked spiral translocation through a linear displacement by more than 12 Å from the previous structures, is surrounded by three hydrophobic residues on $S5_{II}$, Ile876, Ile879, and Phe880 (Fig. 6*B*, *Left*). Substitution of Phe with Ser may weaken the interaction of $S4_I$ with these hydrophobic residues and thus lower the energy barrier, equivalent of a less-depolarized voltage, for the upward movement of $S4_I$ upon depolarization.

Another PERYTHM-related mutation that led to left shift of the activation curve is S211P (42). In the previous structures, Ser is on the extracellular tip of $S4_I$ and close to Lys890, a residue on the extended helix of $S5_{II}$. Such conformation cannot explain the left shift of the activation curve by the pathogenic mutation, as Ser→Pro at this position appears to disfavor the up state of VSD_I (Fig. 6*B*, *Right*). In the structure of M11, Ser211, whose Cα atom moves down by ∼10 Å, points to the hydrophilic interior of VSD_I (Fig. 6*B*). S211P may thus facilitate activation by destabilizing the hydrophilic cluster in the down state of VSD_I. It is noted that the Ser211-coordinating residue Asn209 is close to Gln886 on $S5_{II}$. Q886E is also a PERYTHM-related mutation, although its main disease-causing mechanism may be attributed to its increased stabilizing power of Arg214 (R2) in the up state (Fig. 6*B*).

In addition to the interface between VSD_I and the PD, four of the five hydrophobic residues that mediate the coupling between $S4\text{-}5_I$ and $S5_{II}$ are susceptible to disease-related mutations (Fig. 5*C*). $Na_v1.7$ variants, I234T, L869F, and L869H, are found in patients with PERYTHM (43, 44). In addition to pain-related mutations in $Na_v1.7$, a $Na_v1.5$ variant, V240M (equivalent of V235M in $Na_v1.7$), has been identified in patients with Brugada syndrome or type 3 long QT syndrome (23, 24, 45). Substitutions of $Na_v1.1$-Val896 (equivalent of $Na_v1.7$-Val872) with bulkier residues, Phe, Ile, or Leu, are associated with different forms

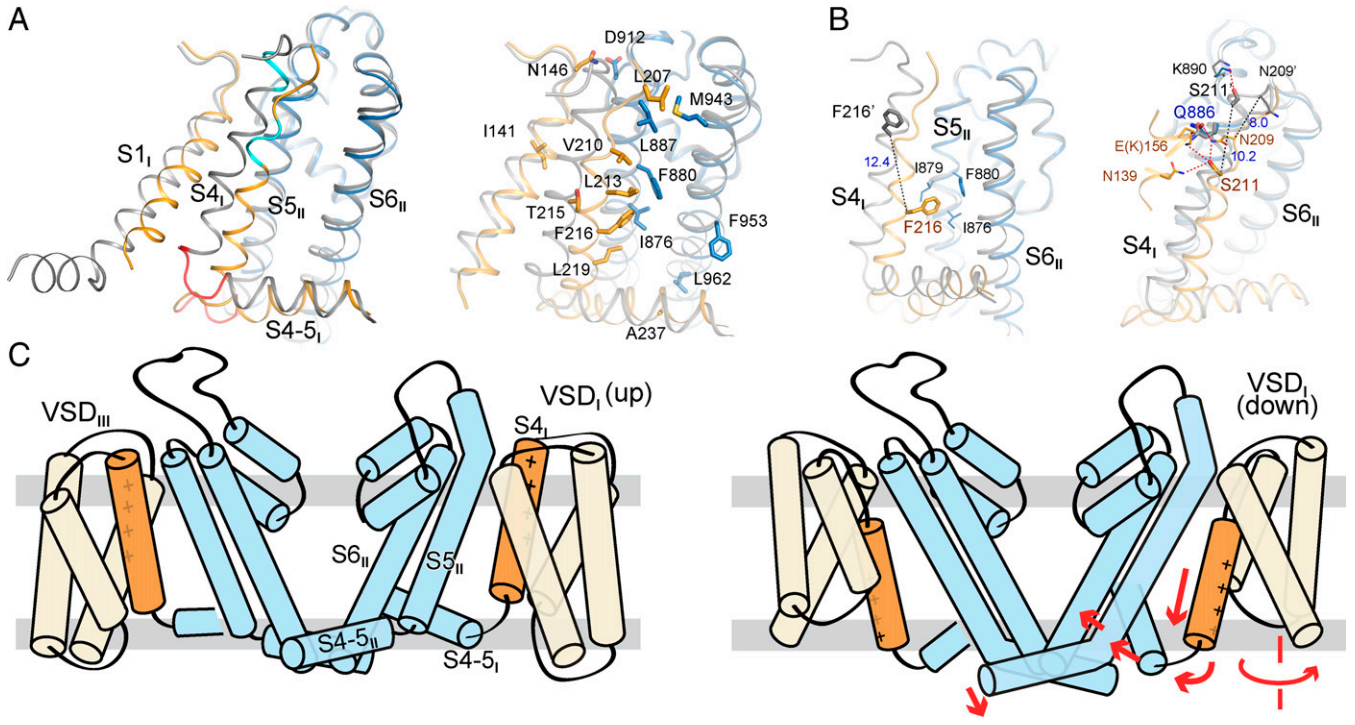

Fig. 6. Structural interpretation of representative $Na_v1.7$ mutations related to pain disorders. (*A*) Rearrangement of the interface between VSD_I and the PD. (*Right*) More residues are engaged in the interactions of the down VSD_I with $S5_{II}$ and $S6_{II}$. Shown here are the additional residues that mediate the VSD_I–PD interface in $Na_v1.7$-M11. Please refer to *SI Appendix*, Fig. S7 for detailed comparison of the VSD_I–PD interface in WT and M11. (*B*) Mechanistic interpretation for representative primary erythermalgia mutations that map to the interface of $S4_I$ and $S5_{II}$. (*Left*) F216S may destabilize the interaction between the down VSD_I and $S5_{II}$. (*Right*) S211P and Q886E may both alter the interactions between the down VSD_I and the PD. Residues in WT are labeled with apostrophe. (*C*) A schematic summary of the propagation of conformational changes for EMC when VSD_I moves down. The WT and M11 structures likely represent the conformations of OSI and CSI, respectively.

of epileptic seizures (23). These pathogenic mutations support the structurally-revealed key role of this conserved hydrophobic cluster in EMC.

Closed-State Inactivation. $Na_v1.7$-M11 activates only when the membrane voltage is above 30 mV (Fig. 1*C*). No current was ever recorded when the preholding potential was set to 0 mV. Therefore, the structure of $Na_v1.7$-M11 should represent the CSI conformation. The structure is largely consistent with previous reports of activated VSD_{III} and VSD_{IV}, deactivated VSD_I and VSD_{II}, and a closed pore for CSI of Na_v channels. Although VSD_{II} is not completely deactivated, it can be related to voltage-dependent conformations associated with CSI (34).

Our recently reported structure of human $Ca_v2.2$ also has VSD_{II} down and the other VSDs up (46). While we were performing more comprehensive experiments before assigning a functional state for that structure, Dong et al. (47) defined it as the CSI state. Indeed, the structures of $Ca_v2.2$ and $Na_v1.7$-M11 share common features of one deactivated VSD and tightly closed PD. Other Na_v and Ca_v channels structures that are featured with all up VSDs and loosely closed PD likely correspond to the OSI conformation.

Our original goal was to capture the structure of $Na_v1.7$ in the resting state; M11 represents a milestone toward this goal. Structural comparison of WT and M11 affords unprecedented insight into the EMC mechanism (Fig. 6*C*). Our present study exemplifies the importance of structural resolution of Na_v channels in different states, as the functional significance of many residues may not be clear in one conformation. Only in the structure of M11 did we discover the conserved WNΦΦD motif (Fig. 2*D*) and the coupling cluster between $S4\text{-}5_I$ and $S5_{II}$ (Fig. 5*C*), and establish the structure–function relationship of a number of pathogenic mutations (Fig. 6*B*). These characterizations lay the foundation to dissect the delicate EMC process of the asymmetric, single-chain Na_v as well as Ca_v channels and shed light on drug development targeting these channels.

Data Availability. Cryo-EM maps and structural model data have been deposited in the Electron Microscopy Database, https://www.ebi.ac.uk/emdb/ (EMDB codes EMD-33484 and EMD-33485) (51, 52) and the Protein Data Bank, http://www.wwpdb.org (PDB ID codes 7XVE and 7XVF) (53, 54).

ACKNOWLEDGMENTS. We thank Xiaomin Li, Fan Yang, and Jianlin Lei for technical support during electron microscopy image acquisition; The Tsinghua University Branch of the China National Center for Protein Sciences (Beijing) for supporting the cryoelectron microscopy facility; and the computational facility support from Tsinghua University Branch of China National Center for Protein Sciences (Beijing). This work was funded by Beijing Nova Program (Z191100001119127) from Beijing Municipal Science and Technology Commission. N.Y. has been supported by the Shirley M. Tilghman endowed professorship from Princeton University since 2017.

Author affiliations: [a]Westlake Laboratory of Life Sciences and Biomedicine, Key Laboratory of Structural Biology of Zhejiang Province, School of Life Sciences, Westlake University, Hangzhou 310024, China; [b]Institute of Biology, Westlake Institute for Advanced Study, Hangzhou 310024, China; and [c]State Key Laboratory of Membrane Biology, Beijing Advanced Innovation Center for Structural Biology, Tsinghua-Peking Joint Center for Life Sciences, School of Life Sciences, Tsinghua University, Beijing 100084, China

1. N. Klugbauer, L. Lacinova, V. Flockerzi, F. Hofmann, Structure and functional expression of a new member of the tetrodotoxin-sensitive voltage-activated sodium channel family from human neuroendocrine cells. *EMBO J.* **14**, 1084–1090 (1995).
2. Y. Yang *et al.*, Mutations in SCN9A, encoding a sodium channel alpha subunit, in patients with primary erythermalgia. *J. Med. Genet.* **41**, 171–174 (2004).
3. M. A. Nassar *et al.*, Nociceptor-specific gene deletion reveals a major role for Nav1.7 (PN1) in acute and inflammatory pain. *Proc. Natl. Acad. Sci. U.S.A.* **101**, 12706–12711 (2004).
4. T. R. Cummins, S. D. Dib-Hajj, S. G. Waxman, Electrophysiological properties of mutant Nav1.7 sodium channels in a painful inherited neuropathy. *J. Neurosci.* **24**, 8232–8236 (2004).
5. J. J. Cox *et al.*, An SCN9A channelopathy causes congenital inability to experience pain. *Nature* **444**, 894–898 (2006).
6. D. L. Bennett, C. G. Woods, Painful and painless channelopathies. *Lancet Neurol.* **13**, 587–599 (2014).
7. M. Alsaloum, G. P. Higerd, P. R. Effraim, S. G. Waxman, Status of peripheral sodium channel blockers for non-addictive pain treatment. *Nat. Rev. Neurol.* **16**, 689–705 (2020).
8. D. Ren *et al.*, A prokaryotic voltage-gated sodium channel. *Science* **294**, 2372–2375 (2001).
9. F. H. Yu, V. Yarov-Yarovoy, G. A. Gutman, W. A. Catterall, Overview of molecular relationships in the voltage-gated ion channel superfamily. *Pharmacol. Rev.* **57**, 387–395 (2005).
10. S. B. Long, E. B. Campbell, R. Mackinnon, Crystal structure of a mammalian voltage-dependent Shaker family K+ channel. *Science* **309**, 897–903 (2005).
11. F. Bezanilla, Gating currents. *J. Gen. Physiol.* **150**, 911–932 (2018).
12. C. M. Armstrong, F. Bezanilla, Charge movement associated with the opening and closing of the activation gates of the Na channels. *J. Gen. Physiol.* **63**, 533–552 (1974).
13. N. Yang, A. L. George Jr., R. Horn, Molecular basis of charge movement in voltage-gated sodium channels. *Neuron* **16**, 113–122 (1996).
14. S. B. Long, E. B. Campbell, R. Mackinnon, Voltage sensor of Kv1.2: Structural basis of electromechanical coupling. *Science* **309**, 903–908 (2005).
15. C. A. Ahern, J. Payandeh, F. Bosmans, B. Chanda, The hitchhiker's guide to the voltage-gated sodium channel galaxy. *J. Gen. Physiol.* **147**, 1–24 (2016).
16. V. Yarov-Yarovoy *et al.*, Structural basis for gating charge movement in the voltage sensor of a sodium channel. *Proc. Natl. Acad. Sci. U.S.A.* **109**, E93–E102 (2012).
17. J. W. West *et al.*, A cluster of hydrophobic amino acid residues required for fast Na(+)-channel inactivation. *Proc. Natl. Acad. Sci. U.S.A.* **89**, 10910–10914 (1992).
18. Z. Yan *et al.*, Structure of the $Na_v1.4$-β1 complex from electric eel. *Cell* **170**, 470–482.e11 (2017).
19. X. Pan *et al.*, Structure of the human voltage-gated sodium channel Nav1.4 in complex with beta1. *Science* **362**, eaau2486 (2018).
20. X. Pan *et al.*, Molecular basis for pore blockade of human Na(+) channel Nav1.2 by the mu-conotoxin KIIIA. *Science* **363**, 1309–1313 (2019).
21. H. Shen, D. Liu, K. Wu, J. Lei, N. Yan, Structures of human Nav1.7 channel in complex with auxiliary subunits and animal toxins. *Science* **363**, 1303–1308 (2019).
22. D. Jiang *et al.*, Structure of the cardiac sodium channel. *Cell* **180**, 122–134.e10 (2020).
23. X. Pan *et al.*, Comparative structural analysis of human Nav1.1 and Nav1.5 reveals mutational hotspots for sodium channelopathies. *Proc. Natl. Acad. Sci. U.S.A.*. **118**, e2100066118 (2021).
24. Z. Li *et al.*, Structure of human Nav1.5 reveals the fast inactivation-related segments as a mutational hotspot for the long QT syndrome. *Proc. Natl. Acad. Sci. U.S.A.* **118**, e2100069118 (2021).
25. Z. Li *et al.*, Structural basis for pore blockade of the human cardiac sodium channel Nav1.5 by the antiarrhythmic drug quinidine. *Angew. Chem. Int. Ed. Engl.* (2021).
26. G. Huang *et al.*, High-resolution structures of human $Na_v1.7$ reveal gating modulation through α-π helical transition of $S6_{IV}$. *Cell Rep.* **39**, 110735 (2022).
27. H. Shen *et al.*, Structure of a eukaryotic voltage-gated sodium channel at near-atomic resolution. *Science* **355**, eaal4326 (2017).
28. T. Clairfeuille *et al.*, Structural basis of α-scorpion toxin action on Na_v channels. *Science* **363**, eaav8573 (2019).
29. D. Jiang *et al.*, Structural basis for voltage-sensor trapping of the cardiac sodium channel by a deathstalker scorpion toxin. *Nat. Commun.* **12**, 128 (2021).
30. H. Shen *et al.*, Structural basis for the modulation of voltage-gated sodium channels by animal toxins. *Science* **362**, eaau2596 (2018).
31. J. P. Smits *et al.*, A mutation in the human cardiac sodium channel (E161K) contributes to sick sinus syndrome, conduction disease and Brugada syndrome in two families. *J. Mol. Cell. Cardiol.* **38**, 969–981 (2005).
32. F. Potet *et al.*, Novel Brugada SCN5A mutation leading to ST segment elevation in the inferior or the right precordial leads. *J. Cardiovasc. Electrophysiol.* **14**, 200–203 (2003).
33. B. P. Bean, Sodium channel inactivation in the crayfish giant axon. Must channels open before inactivating? *Biophys. J.* **35**, 595–614 (1981).
34. P. Angsutararux, P. W. Kang, W. Zhu, J. R. Silva, Conformations of voltage-sensing domain III differentially define NaV channel closed- and open-state inactivation. *J. Gen. Physiol.* **153**, e202112891 (2021).
35. X. Huang *et al.*, Structural basis for high-voltage activation and subtype-specific inhibition of human Nav1.8. *Proc. Natl. Acad. Sci. U.S.A.* (2022), 10.1073/pnas.2208211119.
36. X. Tao, A. Lee, W. Limapichat, D. A. Dougherty, R. MacKinnon, A gating charge transfer center in voltage sensors. *Science* **328**, 67–73 (2010).
37. J. W. Wang *et al.*; Epilepsy Genetic Study Group Japan, Prevalence of SCN1A mutations in children with suspected Dravet syndrome and intractable childhood epilepsy. *Epilepsy Res.* **102**, 195–200 (2012).
38. C. Depienne *et al.*, Spectrum of SCN1A gene mutations associated with Dravet syndrome: Analysis of 333 patients. *J. Med. Genet.* **46**, 183–191 (2009).
39. M. M. Mancardi *et al.*, Familial occurrence of febrile seizures and epilepsy in severe myoclonic epilepsy of infancy (SMEI) patients with SCN1A mutations. *Epilepsia* **47**, 1629–1635 (2006).
40. S. E. Heron *et al.*, De novo SCN1A mutations in Dravet syndrome and related epileptic encephalopathies are largely of paternal origin. *J. Med. Genet.* **47**, 137–141 (2010).
41. J. S. Choi, S. D. Dib-Hajj, S. G. Waxman, Inherited erythermalgia: Limb pain from an S4 charge-neutral Na channelopathy. *Neurology* **67**, 1563–1567 (2006).
42. M. Estacion *et al.*, Can robots patch-clamp as well as humans? Characterization of a novel sodium channel mutation. *J. Physiol.* **588**, 1915–1927 (2010).
43. H. S. Ahn *et al.*, A new Nav1.7 sodium channel mutation I234T in a child with severe pain. *Eur. J. Pain* **14**, 944–950 (2010).
44. W. Huang, M. Liu, S. F. Yan, N. Yan, Structure-based assessment of disease-related mutations in human voltage-gated sodium channels. *Protein Cell* **8**, 401–438 (2017).
45. A. Fatima *et al.*, The disease-specific phenotype in cardiomyocytes derived from induced pluripotent stem cells of two long QT syndrome type 3 patients. *PLoS One* **8**, e83005 (2013).
46. S. Gao, X. Yao, N. Yan, Structure of human $Ca_v2.2$ channel blocked by the painkiller ziconotide. *Nature* **596**, 143–147 (2021).
47. Y. Dong *et al.*, Closed-state inactivation and pore-blocker modulation mechanisms of human $Ca_v2.2$. *Cell Rep.* **37**, 109931 (2021).

48. E. F. Pettersen *et al.*, UCSF Chimera–A visualization system for exploratory research and analysis. *J. Comput. Chem.* **25**, 1605–1612 (2004).
49. W. L. DeLano, The PyMOL Molecular Graphics System (Delano Scientific, San Carlos, CA, 2002). PyMOL 2.5.2. http://pymol.org/2/. Accessed 16 March 2022.
50. O. S. Smart, J. G. Neduvelil, X. Wang, B. A. Wallace, M. S. Sansom, HOLE: A program for the analysis of the pore dimensions of ion channel structural models. *J. Mol. Graph.* **14**, 354–360, 376 (1996).
51. G. Huang *et al.*, Data from "Unwinding and spiral sliding of S4 and domain rotation of VSD during the electromechanical coupling in $Na_v1.7$." Electron Microscopy Database. http://www.ebi.ac.uk/pdbe-srv/emsearch/atlas/33484_summary.html. Deposited 22 May 2022.
52. G. Huang *et al.*, Data from "Unwinding and spiral sliding of S4 and domain rotation of VSD during the electromechanical coupling in $Na_v1.7$." Electron Microscopy Database. http://www.ebi.ac.uk/pdbe-srv/emsearch/atlas/33485_summary.html. Deposited 22 May 2022.
53. G. Huang *et al.*, Data from "Unwinding and spiral sliding of S4 and domain rotation of VSD during the electromechanical coupling in $Na_v1.7$." Protein Data Bank. http://www.rcsb.org/pdb/explore/explore.do?structureId=7XVE. Deposited 22 May 2022.
54. G. Huang *et al.*, Data from "Unwinding and spiral sliding of S4 and domain rotation of VSD during the electromechanical coupling in $Na_v1.7$." Protein Data Bank. http://www.rcsb.org/pdb/explore/explore.do?structureId=7XVF. Deposited 22 May 2022.